
X-ray spectra of Sgr A East and diffuse X-ray background near the Galactic center

Akiko ONO¹, Hideki UCHIYAMA^{2*}, Shigeo YAMAUCHI¹, Masayoshi NOBUKAWA³, Kumiko K. NOBUKAWA¹, and Katsuji KOYAMA⁴

¹Department of Physics, Nara Women's University, Kitauoyanishimachi, Nara 630-8506

²Faculty of Education, Shizuoka University, 836 Ohya, Suruga-ku, Shizuoka 422-8529

³Faculty of Education, Nara University of Education, Takabatake-cho, Nara 630-8528

⁴Department of Physics, Graduate School of Science, Kyoto University, Kitashirakawa-oiwake-cho, Sakyo-ku, Kyoto 606-8502

*E-mail: uchiyama.hideki@shizuoka.ac.jp

Received ; Accepted

Abstract

This paper reports the analysis procedure and results of simultaneous spectral fits of the Suzaku archive data for Sagittarius (Sgr) A East and the nearby Galactic center X-ray emission (GCXE). The results are that the mixed-morphology supernova remnant Sgr A East has a recombining plasma (RP) with Cr and Mn He α lines, and a power-law component (PL) with an Fe I K α line. The nearby GCXE has a ~ 1.5 -times larger surface brightness than the mean GCXE far from Sgr A East, although the spectral shape is almost identical. Based on these results, we interpret that the origins of the RP and the PL with the Fe I K α line are past big flares of Sgr A*.

Key words: ISM: individual objects: Sagittarius A East — ISM: supernova remnants — Galaxy: center — X-rays: ISM — X-rays: diffuse background

1 Introduction

Sagittarius (Sgr) A East is a non-thermal radio shell, a radio supernova remnant (SNR) (Ekers et al. 1983). In the shell, there are other objects, the compact non-thermal radio source (Sgr A*), central massive black hole, spiral-shaped thermal gas streams and central star cluster (Sgr A West). These sources may closely couple with Sgr A East, hence the origin of Sgr A East has been extensively studied. In the X-ray band, the Sgr A East spectrum is composed of 2-temperature collisional ionization equilibrium (CIE) plasmas, with ~ 1 keV and $\sim 5\text{--}7$ keV (Sakano et al. 2004; Park et al. 2005; Koyama et al. 2007b). The abundances are larger than the solar and heavy elements are spatially concentrated in the center. The mass of the progenitor star is estimated to be $13\text{--}20 M_{\odot}$ (e.g., Maeda et al. 2002). The age is $\sim 10^3\text{--}10^4$ years, and hence a young-middle aged SNR of a core-collapsed supernova (CC SN). It is classified as a mixed-morphology SNR (Rho & Petre 1998). In addition to the two thermal plasmas, a non-thermal power-law component (PL) is found in the Suzaku spectrum (Koyama et al. 2007b).

The major X-ray background near Sgr A East is the Galactic center X-ray emission (GCXE) (Koyama et al. 2007b; Koyama 2018), which is composed with the low temperature plasma (LTP) in the $\sim 2\text{--}5$ keV band, high temperature plasma (HTP) and PL associated by Fe I $K\alpha$ line in the $\sim 5\text{--}10$ keV band. The mean spectrum of the latter two components has the equivalent width (EW) of the Fe I $K\alpha$ (at 6.4 keV) and Fe XXV $\text{He}\alpha$ (at 6.7 keV) lines (hereafter EW6.4 and EW6.7) of ~ 180 eV and ~ 510 eV, respectively. The global spectrum is given by a ~ 14 keV temperature plasma with the Fe abundance of ~ 1.2 solar (Nobukawa et al. 2016), or the latter components of a ~ 7.4 keV plasma with the Fe abundance of ~ 1.25 solar associated with a PL of photon index ~ 2 together with the Fe I $K\alpha$ line (Uchiyama et al. 2013). To avoid confusion of the GCXE background, we define the terminologies; “the nearby GCXE” is the GCXE in the 3/4 ring (the white dashed line in figure 1), and “the background GCXE” is the GCXE in the same area of Sgr A East (the white solid circle in figure 1). Thus, real background for Sgr A East is “the background GCXE”. However, the spectrum and flux of the background GCXE has not been yet determined by Chandra (Park et al. 2005), XMM (Sakano et al. 2004) or Suzaku (Koyama 2018).

The spectrum of the nearby GCXE reported by XMM-Newton and Chandra is significantly different from the mean GCXE; typically, the EW6.4 and EW6.7 are ~ 220 eV and ~ 730 eV, respectively (Heard & Warwick 2013), or the Fe abundance is ~ 0.7 solar (Muno et al. 2004). Also, the nearby GCXE has a larger surface brightness (Uchiyama et al. 2013; Heard & Warwick 2013) than the mean GCXE. Therefore, proper estimation of the nearby GCXE is essential to determine a reliable spectrum of Sgr A East. For this requirement, we apply a new analysis procedure of simultaneous

fit with Sgr A East and the nearby GCXE, paying particular attention to the energy band of the Fe K-shell complex.

In spite of well studied HTP plasma, the LTP in the GCXE is less certain than the HTP (e.g., Yamauchi et al. 2018). We therefore ignore the spectrum in the energy band below 2.36 keV and focus on the HTP of the 5–10 keV band. The energy band of 2.36–5 keV, which includes the key line S XVI He α (Uchiyama et al. 2013), is used for the qualitative estimate of the contribution of the LTP to the 5–10 keV band. In this paper, the distance to Sgr A * is 8 kpc (e.g., Reid 1993; Gillessen et al. 2009), and quoted errors are in the 90 % confidence limits.

2 Observations

Survey observations in the Galactic Center region were carried out with the X-ray Imaging Spectrometer (XIS: Koyama et al. 2007a) onboard the Suzaku satellite (Mitsuda et al. 2007). The XISs were composed of 4 CCD cameras placed on the focal planes of the thin foil X-ray Telescopes (XRT: Serlemitsos et al. 2007). XIS 1 employed a back-side illuminated (BI) CCD, while XIS 0, 2, and 3 have front-side illuminated (FI) CCDs. The field of view (FOV) of the XIS was $17'8 \times 17'8$. The observation log is listed in table 1.

Since the spectral resolution of the XIS was degraded due to the radiation of cosmic particles, the spaced-row charge injection (SCI) technique was applied to restore the XIS performance (Uchiyama et al. 2009). The effective observation time of Sgr A East is ~ 240 ks, which is far longer than that in the previous Suzaku report (Koyama et al. 2007b).

3 Analysis and Results

3.1 Data Reduction

The XIS data in the South Atlantic Anomaly, during the earth occultation, and at the low elevation angle from the earth rim of $< 5^\circ$ (night earth) and $< 20^\circ$ (day earth) are excluded. Removing hot and flickering pixels, the data of the Grade 0, 2, 3, 4, and 6 are used. The XIS pulse-height data are converted to Pulse Invariant (PI) channels using the `xispi` software in the HEAsoft 6.19, and the calibration database version 2016-06-07. Figure 1 is the X-ray image of the 6.55–6.80 keV band in the area of Sgr A East and the nearby GCXE, where the non X-ray background (NXB) by `xisnxbgen` (Tawa et al. 2008) is subtracted. The color image and the green solid contours show the Suzaku image. These are similar to the smoothed Chandra image and the XMM image (see, figure 2e of Maeda et al. 2002, and figure 1c of Sakano et al. 2004). The spectra are made from the areas of the $1'6$ radius circle (hereafter, the Sgr A East area) and the $3/4$ ring of $3'0 - 5'0$ radius around Sgr A * excluding eastern

Table 1. List of data used for spectral analyses.

Observation ID	Pointing position		Observation time (UT)		Exposure time* (ks)	Spectrum [†]
	$l(^{\circ})$	$b(^{\circ})$	Start	End		
100027010	0.057	−0.074	2005-09-23 07:18:25	2005-09-24 11:05:19	44.8	Sgr A East / GCXE
100037040	0.057	−0.074	2005-09-30 07:43:01	2005-10-01 06:21:24	42.9	Sgr A East / GCXE
100048010	0.057	−0.074	2006-09-08 02:23:24	2006-09-09 09:06:15	63.0	Sgr A East / GCXE
100027020	−0.247	−0.046	2005-09-24 14:17:17	2005-09-25 17:27:19	42.8	Sgr A East / GCXE
100037010	−0.247	−0.046	2005-09-29 04:35:41	2005-09-30 04:29:19	43.7	Sgr A East / GCXE
501008010	−0.154	−0.191	2006-09-26 14:18:16	2006-09-29 21:25:14	129.6	GCXE
501009010	−0.074	0.178	2006-09-29 21:26:07	2006-10-01 06:55:19	51.2	GCXE

* Effective exposure time after screening described in text.

[†] This column shows whether the data were used to make Sgr A East or the nearby GCXE spectrum.

bright X-ray reflection nebula (XRN) regions (Park et al. 2004; Koyama 2018, references therein) (hereafter, the nearby GCXE area), respectively (see figure 1).

3.2 Model Spectra of the Nearby GCXE and Sgr A East

Our main objective is spectral analysis in the Fe K-shell band (the ~ 5 –10 keV band), both for the nearby GCXE and Sgr A East. Accordingly, we ignore the energy band below 2.36 keV in the following spectral analysis. The GCXE has been known to be composed of several different class of sources (e.g., Koyama 2018), and the spectrum has been successfully modeled by high and low temperature CIE plasmas (HTP and LTP), with linked abundances for the both plasma¹. In addition, a PL with Fe I K lines is included. In the analysis of both the nearby GCXE and Sgr A East spectra, the cosmic X-ray background (CXB) compiled by Kushino et al. (2002) is included.

The model spectrum of Sgr A East is assumed to be a combination of ejecta and interstellar medium (ISM). We try two fits with the ISM models which are either a \sim solar abundances plasma, or a plasma with same abundances as the those of the diffuse plasma of the nearby GCXE. No essential difference between these two fits is found. This paper refers to the results of the latter case, because Sgr A East is located in the GCXE, which would be largely affected by Sgr A* activity, high star burst activity, strong magnetic field and etc, and hence usual ISM with \sim solar abundance may not be

¹ Since the GCXE is composed of many classes of sources with different temperatures and abundances (Koyama 2018), assuming an average value of the estimated abundances for each element for both spectral components would be reasonable.

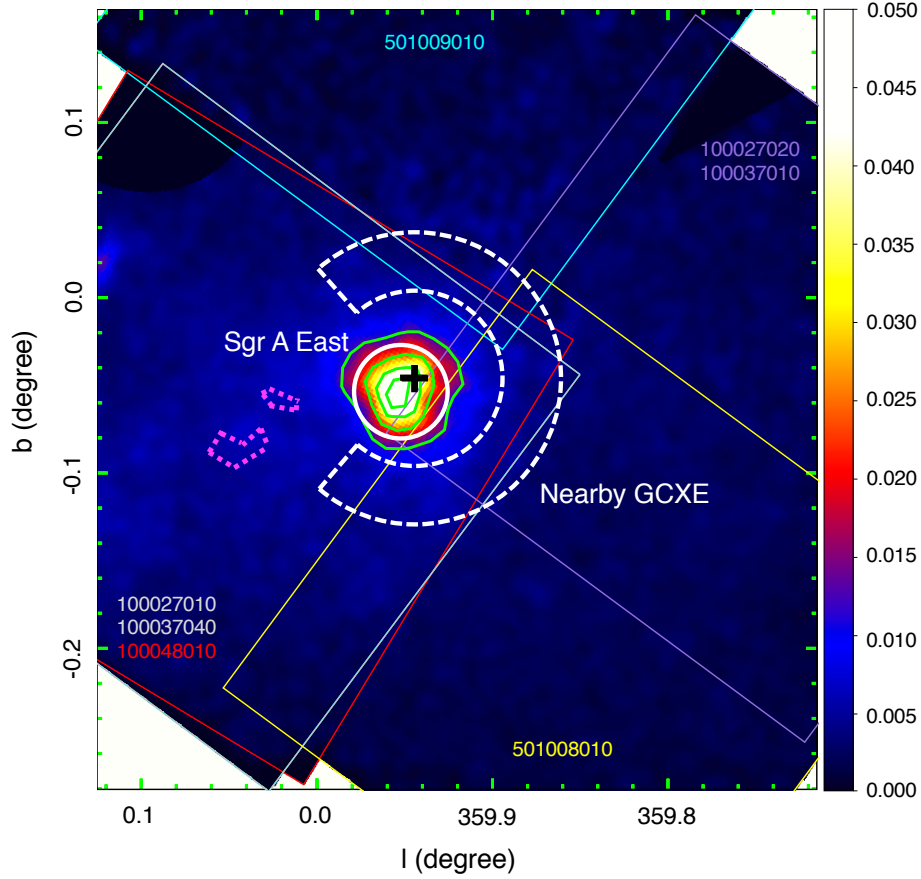


Fig. 1. The 6.55–6.80 keV band (Fe K-shell line complex) image of XIS in the Galactic coordinate. The color image and the green solid contours show the Suzaku image. The color bar is X-ray surface brightness of liner scale in arbitrary unit. The brightest region shown by the white solid circle is the Sgr A East area, while the 3/4 ring with the white dashed line is the nearby GCXE area. The black cross shows the position of Sgr A*. The magenta dotted lines show the regions of bright XRNe found by Chandra (Park et al. 2004; filament 1 and 2). The nearby GCXE and Sgr A East are out of the XRN regions. The borders of the field of view (FOV) of each observations (table 1) are separately shown by the gray, red, purple, cyan, and yellow lines, where those of ID100027010 and ID100037040, (also ID100027020 and ID100037010) are overlapped.

applied.

3.3 Simultaneous Fit of Sgr A East with the Nearby GCXE

The process of simultaneous-fit is analogous to solving simultaneous equations of $aX + bY = A$, and $cX + dY = B$, where X and Y are model functions of Sgr A East and GCXE, and A and B are observed spectra from the Sgr A East area and the nearby GCXE area. The constant parameters of a, b, c , and d correspond to effective areas given by ARFs², ARF-1, 2, 3 and 4. ARF-1 and ARF-2 are made using the Chandra image of Sgr A East (Maeda et al. 2002; Park et al. 2005). ARF-3 and ARF-4 are made from the Fe XXV He α distribution within 5' from Sgr A* (Heard & Warwick 2013) of

² Ancillary Response File (ARF) describes energy-dependent effective area which is calculated from the spatial distribution of the source and the photon accumulation region on the detector under the XRT response and contamination of the optical blocking filter (Ishisaki et al. 2007).

a 2-exponential function with e-folding longitude and latitude of $11'$ and $9'$, respectively. The fluxes of Sgr A East and the GCXE in the Sgr A East area are determined by ARF-1 and ARF-3 (parameters a , and b), while those in the nearby GCXE area are determined by ARF-2 and ARF-4 (parameters c , and d), respectively. The spectral parameters and fluxes of X and Y depend on both of A and B . Therefore, all the relevant parameters are coupled with each other complicatedly. The simultaneous fit with multiple ARFs can determine these parameters separately by χ^2 minimizing process, which is essential point of this fitting method.

The GCXE background by many previous authors (e.g., Sakano et al. 2004; Maeda et al. 2002) were taken from the region around the nearby GCXE, not from the background GCXE of Sgr A East. Hence, their GCXE backgrounds were always underestimated, because the surface brightness of the GCXE near Sgr A East ($\lesssim 10'$ radius) shows significant increase toward Sgr A* (Heard & Warwick 2013). In fact, the surface brightness of the nearby GCXE and the background GCXE are estimated to be 2.4×10^{-13} and 3.5×10^{-13} erg s $^{-1}$ cm $^{-2}$ arcmin $^{-2}$ (5–10 keV), respectively. In our simultaneous fit, the ARF takes account of the spatially distribution of the GCXE. Thus, the spectra and fluxes of the background GCXE and the nearby GCXE should be reliably estimated, in particular in the high energy band (5–10 keV) features of Fe peaked elements. As is shown in figure 1, each pointing position (Observation ID) of table 1 covers only a fraction of the nearby GCXE area. Therefore, the unit of the vertical axis (counts s $^{-1}$ keV $^{-1}$) in figure 2c is not proportional to the flux of the full nearby GCXE area (the 3/4 ring). The effective area is calculated using ARFs generated with `xissimarfgen` (Ishisaki et al. 2007), and is $\sim 45\%$ of the full 3/4 ring area.

At first, we assume that Sgr A East spectrum is a composite of two CIE plasma, which represent the ejecta and ISM plasma (Sakano et al. 2004; Park et al. 2005; Koyama et al. 2007b). This two CIE model assumes ~ 1 solar abundances of Mn and Cr, which is a same model as those of commonly used and accepted previously (e.g., Sakano et al. 2004; Park et al. 2005). The simultaneous fit reveals that the two CIE model shows clear excess at the energies of Mn and Cr, indicating that Mn and Cr are over abundant (> 1 solar). We also find excess at 6.4 keV of Fe I K α line (see figure 2a). Adding a PL plus Fe I K component with free parameter of equivalent width, a better fit with $\chi^2/\text{d.o.f.}$ of 286/228=1.25 (null probability is 0.6 %) is obtained. Hereafter, we named this model as the conventional 2-CIE model (in short, 2-CIE). The best-fit 2-CIE model and parameters are given in figure 2a and the 2nd, 3rd columns in table 2, respectively. In figure 2a, we find significant data excesses from the 2-CIE model in the energy band of 5–10 keV, where the radiative recombination continuum (Fe XXV RRC), Cr XXIII He α and Mn XXIV He α exist. The excess of the Fe XXV RRC is direct evidence for the recombining plasma (RP) (e.g., Ohnishi et al. 2014), because the relevant plasma should include significant fraction of Fe XXVI ions, more than that of the CIE plasma.

In order to check the significance of the excesses at the Fe-RRC, Mn and Cr line energies in the 2-CIE model, we apply two RP model (for the residual at Fe-RRC) including Mn and Cr abundances as free parameters (for the residuals at Mn and Cr lines). This two RP model includes the PL with Fe I K lines (here and after, 2-RP model). Then, most of the residuals disappear (see figure 2b) with statistically highly acceptable results of $\chi^2/\text{d.o.f.}=241/224=1.08$. The reduction of the χ^2 value from the 2-CIE to the 2-RP is 45, which is equally shared to the Fe-RRC and Mn, Cr residuals. If we limited the energy band of 5–10 keV, where Fe-RRC and Cr, Mn lines exist, the $\chi^2/\text{d.o.f.}$ of the 2-CIE and 2-RP models are $142/90=1.58$ and $100/86=1.16$, respectively. This large difference also justify to apply the 2-RP model instead of 2-CIE. We further apply the F-test judgment and find significant improvement from the 2-CIE fit ($\chi^2/\text{d.o.f.}=286/228=1.25$) to the 2-RP fit ($\chi^2/\text{d.o.f.}=241/224=1.08$) with more than 99.99 % of null probability. The best-fit Sgr A East and the nearby GCXE spectrum in the case of the 2-RP model are given in figure 2b and 2c, respectively. The best-fit parameters are shown in the 4th and 5th columns of table 2.

4 Discussion

4.1 X-Ray Spectrum of the Nearby GCXE

We find that the nearby GCXE has almost the same temperatures and abundances as those of the mean GCXE (see table 2 and Koyama 2018). These results seem inconsistent with the results of Chandra and XMM-Newton (Muno et al. 2004; Heard & Warwick 2013). The reason of this apparent inconsistency is simple; Muno et al. (2004) and Heard & Warwick (2013) reported that the significant contribution from a PL component was not required to describe the observed X-ray spectrum, while our GCXE has the PL with 46σ significance (see table 2). The nearby GCXE has a high temperature of ~ 7.4 keV with the Fe abundance of ~ 1.25 solar, essentially the same spectrum as, but ~ 1.5 times larger surface brightness than the mean GCXE.

4.2 Contribution of Sgr A* to Sgr A East

The background GCXE is partially composed of many point sources including Sgr A*. The brightest point source Sgr A* has the absorption-corrected luminosity of $2.4 \times 10^{33} \text{ erg s}^{-1}$ (2–10 keV; Baganoff et al. 2003). Using the spectrum parameters of Sgr A* ($\Gamma=2.7$, $N_{\text{H}} = 10^{23} \text{ cm}^{-2}$; Baganoff et al. 2003), it is converted to the absorbed luminosity of $5.8 \times 10^{32} \text{ erg s}^{-1}$ in the 5–10 keV band, which covers the essential energy band of Fe-K lines and RRC of Sgr A East. Sgr A* exhibits weak flares of $< 10^{35} \text{ erg s}^{-1}$ (2–10 keV) with the rate of $\sim 1 \text{ day}^{-1}$ and the flare duration is less than \sim a few ks (Nielsen et al. 2013). The time averaged luminosity is estimated to be in the order of $< 10^{33} \text{ erg s}^{-1}$ (5–10 keV)

Table 2. The best-fit parameters for Sgr A East and the nearby GCXE in the cases of the 2-CIE or 2-RP model for Sgr A East.

	In the case of 2-CIE model for Sgr A East		In the case of 2-RP model for Sgr A East	
	Sgr A East	nearby GCXE	Sgr A East	nearby GCXE
	ISM (CIE)	LTP (CIE)	ISM (RP)	LTP (CIE)
kT_e^*	1.05 ± 0.05	1.04 ± 0.03	0.95 ± 0.10	1.05 ± 0.03
kT_i^*	-	-	10 (fixed)	-
Z_S^\dagger	link to nearby GCXE	link to HTP	link to nearby GCXE	link to HTP
Z_{Ar}^\dagger	link to nearby GCXE	link to HTP	link to nearby GCXE	link to HTP
Z_{Ca}^\dagger	link to nearby GCXE	link to HTP	link to nearby GCXE	link to HTP
$n_e t^\parallel$	-	-	> 17	-
Norm. [#]	0.19 ± 0.03	0.35 ± 0.06	0.19 ± 0.06	0.33 ± 0.03
	Ejecta (CIE)	HTP (CIE)	Ejecta (RP)	HTP (CIE)
kT_e^*	4.5 ± 0.1	7.4 ± 0.2	2.3 ± 0.2	7.4 ± 0.2
kT_i^*	-	-	10 (fixed)	-
Z_S^\dagger	$0.0(< 2.0)$	1.7 ± 0.1	$0.3(< 1.4)$	1.7 ± 0.1
Z_{Ar}^\dagger	$0.8(< 2.4)$	1.3 ± 0.1	$0.4(< 1.0)$	1.4 ± 0.1
Z_{Ca}^\dagger	$0.7(< 1.8)$	1.5 ± 0.1	1.0 ± 0.5	1.6 ± 0.1
Z_{Cr}^\dagger	1.0 (fixed)	1.0 (fixed)	4.4 ± 1.6	1.0 (fixed)
Z_{Mn}^\dagger	1.0 (fixed)	1.0 (fixed)	14 ± 8	1.0 (fixed)
Z_{Fe}^\dagger	1.8 ± 0.4	1.25 ± 0.05	1.5 ± 0.3	1.25 ± 0.05
Z_{Ni}^\dagger	$0.4(< 1.3)$	1.25 (link to Fe)	$1.5(< 3.0)$	1.25 (link to Fe)
$n_e t^\parallel$	-	-	6.3 ± 0.5	-
Norm. [#]	0.013 ± 0.009	0.041 ± 0.001	0.034 ± 0.017	0.041 ± 0.001
	Power law + Fe I K α		Power law + Fe I K α	
Γ	1.0 ± 0.9	1.7 ± 0.1	1.0 ± 0.8	1.7 ± 0.1
PL norm. ^{**}	0.40 ± 0.27	1.95 ± 0.07	0.45 ± 0.22	1.96 ± 0.07
EW6.4 (eV)	200 ± 140	460 (fixed) ^{††}	160 ± 80	460 (fixed) ^{††}
$N_H^{\parallel\parallel\parallel}$	15 ± 1	8.9 ± 0.2	15 ± 1	8.7 ± 0.2
$\chi^2/\text{d.o.f.}$	286/228=1.25		241/224=1.08	

* Units are keV. kT_e is the electron temperature. kT_i is the initial ionization temperature at $n_e t = 0$. [†] Abundances relative to the solar value of Anders & Grevesse (1989). [‡] Unit is $10^{11} \text{ s cm}^{-3}$. [#] Defined as $10^{-14} \times \int n_H n_e dV / (4\pi D^2)$ (cm^{-5}), where n_H , n_e , and D are hydrogen density (cm^{-3}), electron density (cm^{-3}) and distance to Sgr A East (cm), respectively. ^{**} Unit is photons $\text{s}^{-1} \text{ cm}^{-2} \text{ keV}^{-1}$ at 6.4 keV. ^{††} Fixed to the value of the mean GCXE (Uchiyama et al. 2013). ^{‡‡‡} The hydrogen column density of the interstellar absorption in unit of 10^{22} cm^{-2} .

using $\Gamma = 2.3$ (Ponti et al. 2017). The observed luminosity of Sgr A East is $\sim 7 \times 10^{34}$ erg s $^{-1}$ in the 5–10 keV band (Koyama et al. 2007b). Thus, the contribution of both of the stable (non-flare) and time-averaged flare fluxes of Sgr A * is estimated to be at most ~ 3 % of the Sgr A East flux. Although the nominal spatial resolution of XIS is $\sim 1'$, the point spread function has a sharp cusp structure (Serlemitsos et al. 2007), which makes it possible to show a peak position of Sgr A * flare with better than $20''$ accuracy (Uchiyama et al. 2008). The Suzaku image shows no peak nor large enhancement at the position of Sgr A * (see figure 1). Accordingly, the effects of the Sgr A * flux to the spectrum of Sgr A East are negligible.

4.3 X-Ray Spectrum of Sgr A East

We find that the 2-RP model gives better fit than the 2-CIE model to the updated Suzaku spectrum (see figure 2). In addition to the better χ^2 value of the 2-RP model than the 2-CIE model, we preferred the 2-RP model than the 2-CIE model, because the former predicts the presence of the RP, and the He α lines of rare elements, Cr and Mn, and the Fe I K α line in the ejecta plasma for the first time.

The temperature of ~ 4.5 keV in the 2-CIE fit is high even for the young SNR. In fact, the youngest Galactic CC-SNR Cas A has only ~ 2 – 4 keV (Maeda et al. 2009), or has a steep power-law index of ~ 3 (Sato et al. 2017). This high temperature plasma in the 2-CIE fit is reduced to ~ 2.3 keV in the 2-RP fit (the 2nd and 4th columns of table 2), which is more typical temperature for a young-middle aged CC SNR (e.g., Cas A, Maeda et al. 2009). Even this temperature produces Fe XXVI Ly α line, which is another important aspect of the 2-RP model. The abundance pattern of S, Ar, Ca, Fe and Ni of ejecta favors a CC SN origin of the low mass side (Maeda et al. 2002). One may argue that Fe abundance in the ejecta of SNR, is not enhanced (table 2). This seems to be inconsistent with the previous CIE fit. In fact, Park et al. (2005) found that Fe abundance is $5.8^{+1.7}_{-1.1}$ solar at the center. On the other hand, our 2-RP fit gives the average Fe abundance to be 1.5 ± 0.3 solar. This apparent inconsistency is not surprising because the previous work is CIE fit for the Sgr A East spectra with under-estimated GCXE background, but ours is 2-RP fit with the proper subtraction of GCXE background (see the 2nd paragraph of section 3.3). In addition, the Fe abundance of ~ 5.8 solar is the result of the very small ($\sim 20''$) Fe-rich central region (Park et al. 2005). Sakano et al. (2004) and Park et al. (2005) find Fe increases toward the central region of Sgr A East. Our result is the mean abundance of the whole ejecta ($1/6$ -radius region) and naturally smaller than that of the Fe-rich center. We should note that the mean Fe abundance of ~ 1.5 solar is not unreasonable for the ejecta of CC-SNRs.

Due to the low abundance of Mn, Mn XXIV He α lines have been detected from only 6 SNRs

(Yang et al. 2013). Among them, W49B is a unique SNR exhibiting Fe-RRC (e.g., Ozawa et al. 2009). In all of those 6 SNRs, the flux ratios of Mn/Cr are within standard models (e.g., Woosley & Weaver 1995; Sukhbold et al. 2016). Sgr A East, however, has a far larger Mn/Cr ratio, which is out of the standard models. We speculate that Mn is over-produced in a neutron rich region, or in neutron star.

In the mixed-morphology SNR, the current scenario for the origin of the RP is either electron cooling by cold molecular clouds (Kawasaki et al. 2002) or adiabatic expansion through the clouds (Masai 1994) (rarefaction). The 2-RP model requires the initial ionization temperature (kT_i) of ~ 10 keV, which is not obtained by the conventional electron cooling scenario. Therefore, we speculate other possibility, an X-ray photo-ionization of Sgr A^{*} flares, which also explain the presence of Fe I K α line. In this scenario, the structure of RP is determined by the parameter of $\xi = L/(n_e R^2)$ (Kallman et al. 2004), where n_e , R and L are the electron density of the ejecta plasma (cm^{-3}), the distance (cm) from Sgr A^{*} and the luminosity (erg s^{-1}) of the past flare of Sgr A^{*}, respectively. If $\log \xi \gtrsim 4$, the ejecta becomes H-like and naked Fe dominant plasma (RP). From the volume emission measure of the ejecta, n_e is estimated to be $\sim 4 \text{ cm}^{-3}$. Then, with the best-fit $n_e t$ of $6.3 \times 10^{11} \text{ s cm}^{-3}$, $\log \xi = 4$ and $R \sim 1 \text{ pc}$, the time (t) after the photo ionization and flare luminosity (L) are estimated to be $\sim 10^4$ years and $\sim 10^{42} \text{ erg s}^{-1}$, respectively. Thus, in Sgr A East of $R \sim 1 \text{ pc}$, the RP would be produced by Sgr A^{*} flares of $\sim 10^4$ years ago with the luminosity of $L \sim 10^{42} \text{ erg s}^{-1}$. The flare luminosity is in between those of ~ 100 – 800 years ago ($\sim 10^{39} \text{ erg s}^{-1}$; Ryu et al. 2009, 2013) and that of $\sim 10^5$ years ago ($\sim 10^{44} \text{ erg s}^{-1}$; Nakashima et al. 2013).

The PL components are found in both Sgr A East and the nearby GCXE spectra (table 2) with the significance levels of 3.3σ and 46σ , respectively. Munro et al. (2008) reports 12 non-thermal filaments in the Sgr A East area. We make the summed spectrum of the 12 filaments and found that the spectrum is a PL with the luminosity of $7.4 \times 10^{33} \text{ erg s}^{-1}$ (5–10 keV), which is only 24 % of the best-fit PL luminosity of Sgr A East. In the summed spectrum, no significant Fe I K α line is detected. Therefore a major fraction of the PL plus Fe I K α line would be due to undetected components. One speculation is that there are many faint XRNe of small N_H cloudlets, which would be hard to detect with the present instruments.

5 Conclusion

We have performed simultaneous spectral fits for Sgr A East and the nearby GCXE. The results are:

- RRC structure of Fe XXV, and K-shell lines of Cr XXIII He α , Mn XXIV He α and Fe I K α are discovered from Sgr A East.

- The spectrum of Sgr A East is nicely explained by two RP components.
- The origin of the RP is probably due to the past big flares of Sgr A* with the luminosity of $\sim 10^{42}$ erg s $^{-1}$.
- The nearby GCXE has a similar spectrum to the mean GCXE, although the surface brightness is ~ 1.5 times larger than that of the mean GCXE.

Acknowledgement

The authors are grateful to all members of the Suzaku team. This work was supported by the Japan Society for the Promotion of Science (JSPS) KAKENHI Grant Numbers JP25887028 (HU), JP15H02090, JP17K14289 (MN), JP24540232 (SY) and JP16J00548 (KKN) and Nara Women's University Intramural Grant for Project Research (SY).

References

- Anders, E., & Grevesse, N. 1989, *Geochim. Cosmochim. Acta*, 53, 197
- Baganoff, F. K., et al. 2003, *ApJ*, 591, 891
- Ekers, R. D., van Gorkom, J. H., Schwarz, U. J., & Goss, W. M. 1983, *A&A*, 122, 143
- Gillessen, S., Eisenhauer, F., Trippe, S., Alexander, T., Genzel, R., Martins, F., & Ott, T. 2009, *ApJ*, 692, 1075
- Heard, V., & Warwick, R. S. 2013, *MNRAS*, 428, 3462
- Ishisaki, Y., et al. 2007, *PASJ*, 59, 113
- Kallman, T. R., Palmeri, P., Bautista, M. A., Mendoza, C., & Krolik, J. H. 2004, *ApJS*, 155, 675
- Kawasaki, M. T., Ozaki, M., Nagase, F., Masai, K., Ishida, M., & Petre, R. 2002, *ApJ*, 572, 897
- Koyama, K., et al. 2007a, *PASJ*, 59, S23
- Koyama, K., Uchiyama, H., Hyodo, Y., Matsumoto, H., Tsuru, T. G., Ozaki, M., Maeda, Y., & Murakami, H. 2007b, *PASJ*, 59, S237
- Koyama, K. 2018, *PASJ*, 70, 1
- Kushino, A., Ishisaki, Y., Morita, U., Yamasaki, N. Y., Ishida, M., Ohashi, T., & Ueda, Y. 2002, *PASJ*, 54, 327
- Maeda, Y., et al. 2002, *ApJ*, 570, 671
- Maeda, Y., et al. 2009, *PASJ*, 61, 1217
- Masai, K. 1994, *ApJ*, 437, 770
- Mitsuda, K., et al. 2007, *PASJ*, 59, S1
- Muno, M. P., Baganoff, F. K., Bautz, M. W., et al. 2004, *ApJ*, 613, 326
- Muno, M. P., Baganoff, F. K., Brandt, W. N., Morris, M. R., & Starck, J.-L. 2008, *ApJ*, 673, 251

- Nakashima, S., Nobukawa, M., Uchida, H., Tanaka, T., Tsuru, T. G., Koyama, K., Murakami, H., & Uchiyama, H. 2013, *ApJ*, 773, 20
- Neilsen, J., et al. 2013, *ApJ*, 774, 42
- Nobukawa, M., Uchiyama, H., Nobukawa, K. K., Yamauchi, S., & Koyama, K. 2016, *ApJ*, 833, 268
- Ohnishi, T., Uchida, H., Tsuru, T. G., Koyama, K., Masai, K., & Sawada, M. 2014, *ApJ*, 784, 74
- Ozawa, M., Koyama, K., Yamaguchi, H., Masai, K., & Tamagawa, T. 2009, *ApJL*, 706, L71
- Park, S., Munro, M. P., Baganoff, F. K., Maeda, Y., Morris, M., Howard, C., Bautz, M. W., & Garmire, G. P. 2004, *ApJ*, 603, 548
- Park, S., et al. 2005, *ApJ*, 631, 964
- Ponti, G., et al. 2017, *MNRAS*, 468, 2447
- Reid, M. J. 1993, *ARA&A*, 31, 345
- Rho, J., & Petre R. 1998, *ApJ*, 503, L167
- Ryu, S. G., Koyama, K., Nobukawa, M., Fukuoka, R., & Tsuru, T. G. 2009, *PASJ*, 61, 751
- Ryu, S. G., Nobukawa, M., Nakashima, S., Tsuru, T. G., Koyama, K., & Uchiyama, H. 2013, *PASJ*, 65, 33
- Sakano, M., Warwick, R. S., Decourchelle, A., & Predehl, P. 2004, *MNRAS*, 350, 129
- Sato, T., et al. 2017, *ApJ*, 836, 225
- Serlemitsos, P. J., et al. 2007, *PASJ*, 59, 9
- Sukhbold, T., Ertl, T., Woosley, S. E., Brown, J. M., & Janka, H.-T. 2016, *ApJ*, 821, 38
- Tawa, N., et al. 2008, *PASJ*, 60, S11
- Uchiyama, Y., Maeda, Y., Ebara, M., et al. 2008, *PASJ*, 60, S35
- Uchiyama, H. et al. 2009, *PASJ*, 61, S9
- Uchiyama, H., Nobukawa, M., Tsuru, T. G., & Koyama, K. 2013, *PASJ*, 65, 19
- Woosley, S. E., & Weaver, T. A. 1995, *ApJS*, 101, 181
- Yang, X. J., Tsunemi, H., Lu, F. J., Li, Aigen, Xiang, F. Y., Xiao, H. P., & Zhong, J. X. 2013, *ApJ*, 766, 44
- Yamauchi, S., Shimizu, M., Nobukawa, M., Nobukawa, K. K., Uchiyama, H., & Koyama, K. 2018, *PASJ*, 70,

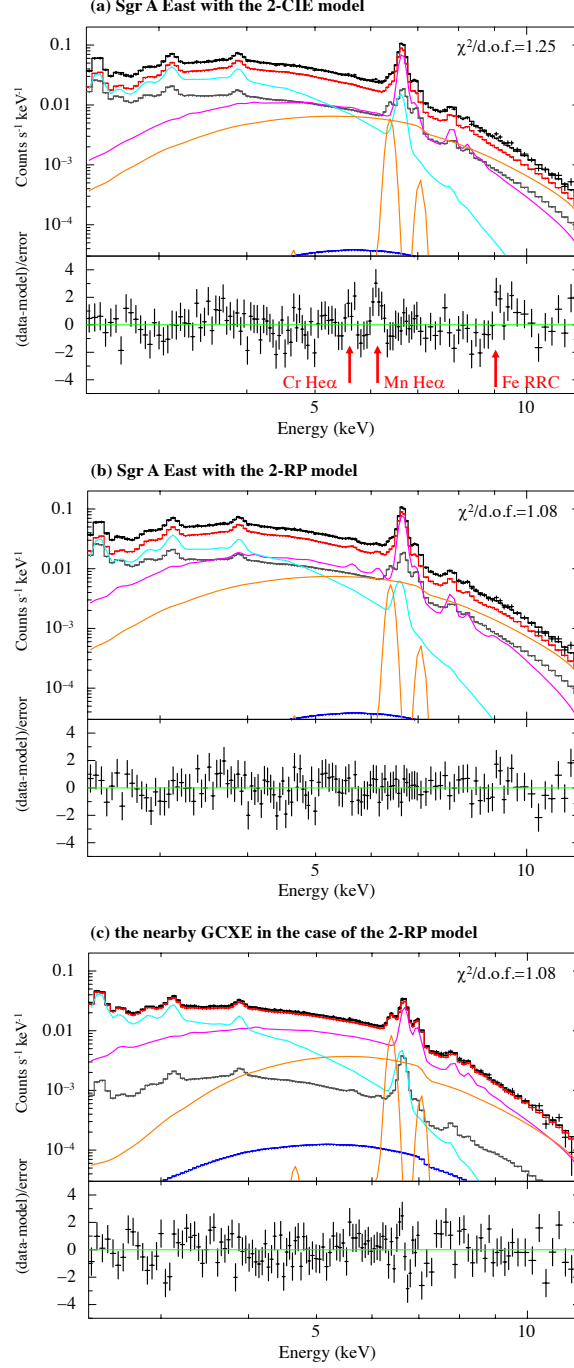


Fig. 2. (a,b) The best-fit Sgr A East models of 2-CIE and 2-RP. The magenta, cyan, orange, blue and gray lines show the ejecta plasma, ISM plasma, PL+Fe I K lines, CXB and “the background GCXE”, respectively. The red line shows the total model of Sgr A East SNR (ejecta+ISM+PL+Fe I K lines). The black line shows the sum of all the model components (Sgr A East SNR+the background GCXE+CXB). (c) The best-fit nearby GCXE model in the case of 2-RP. The magenta, cyan, orange, blue and gray lines show the HTP, LTP, PL+Fe I K lines, CXB and the contamination of Sgr A East, respectively. The red line shows the total model of the nearby GCXE (HTP+LTP+PL+Fe I K lines). The black line shows the sum of all the model components (the nearby GCXE+the contamination of Sgr A East+CXB).